Appl Phys B (2010) 101: 45–56
DOI 10.1007/s00340-010-4050-6

Applied Physics B
Lasers and Optics

A three-level analytic model for alkali metal vapor lasers: part I. Narrowband optical pumping

G.D. Hager · G.P. Perram

Received: 18 December 2009 / Revised version: 16 April 2010 / Published online: 22 May 2010

Abstract A three-level analytic model for optically pumped alkali metal vapor lasers is developed by considering the steady-state rate equations for the longitudinally averaged number densities of the ground $^2S_{1/2}$ and first excited $^2P_{3/2}$, and $^2P_{1/2}$ states. The threshold pump intensity includes both the requirements to fully bleach the pump transition and exceed optical losses, typically about 200 W/cm^2. Slope efficiency depends critically on the fraction of incident photons absorbed and the overlap of pump and resonator modes, approaching the quantum efficiency of 0.95–0.98, depending on the alkali atom. For marginal cavity transmission losses, peak performance is achieved for low output coupling mirror reflectivity. For efficient operation, the collisional relaxation between the two upper levels should be fast to prevent bottlenecking. By assuming a statistical distribution between the upper two levels, the limiting analytic solution for the quasi two-level system is achieved. For properly designed gain conditions, the quasi two-level solution is usually achievable and represents ideal performance.

1 Introduction

A new class of optically pumped lasers has recently been proposed by Krupke et al. [1]; the diode pumped alkali metal vapor laser (DPAL). While an optically pumped cesium laser was demonstrated in 1962 [2], it is only recently that diode laser excitation was proposed [1, 3]. These three-level lasers are pumped on the D_2 line, $^2S_{1/2} \rightarrow ^2P_{3/2}$, and support lasing on the D_1 line, $^2P_{1/2} \rightarrow ^2S_{1/2}$, as shown in Fig. 1. Rapid collision induced spin-orbit relaxation with an additive gas such as methane, typically at a pressure of several hundred torr, populates the lower $^2P_{1/2}$ state. The difference in energy between the $^2P_{3/2}$ and $^2P_{1/2}$ fine structure spin-orbit components is 554 cm^{-1}, 237 cm^{-1}, and 57.7 cm^{-1} for Cs, Rb, and K respectively. These small energy defects lead to intrinsic quantum efficiencies of greater than 95% and to the possibility of very efficient laser systems. The alkali atoms provide very high optical cross sections and offer an efficient engine for converting incoherent, or unphased, pump photons into a coherent, single mode beam. The number density of the alkali atoms in these devices is low, typically 10^{13}–10^{14} atoms per cm^3. Each alkali atom in the laser medium cycles many millions of pump photons per second during the lasing process, providing the promise of high power from small gain volumes.

As with all three-level laser systems, the threshold pumping requirements are high. Matching the diode laser bandwidth with the gas phase absorption line shape either requires high pressure cells, ∼25 atmospheres for the ∼1000 GHz diode bandwidth available for high-power bars and stacks, or narrow-banding the pump source to ∼10 GHz, the width of the Cs D_2 line at 400 torr of helium.

A number of laser demonstrations using this concept with Cs, Rb, and K have appeared recently in the open literature [3–12], and have stimulated a great deal of interest in the high-power laser community. These demonstrations have used single narrowband diodes, partially narrowband low-power diode arrays, and surrogate pump sources such as Ti-Sapphire as pump sources. DPAL devices based on Rb have been demonstrated at 0.4 W with a slope efficiency of 69% and 17 W at 53% efficiency [8, 12]. Similarly, the Cs

G.D. Hager · G.P. Perram (✉)
Department of Engineering Physics, Air Force Institute of Technology, 2950 Hobson Way, Wright-Patterson Air Force Base, OH 45433, USA
e-mail: glen.perram@afit.edu

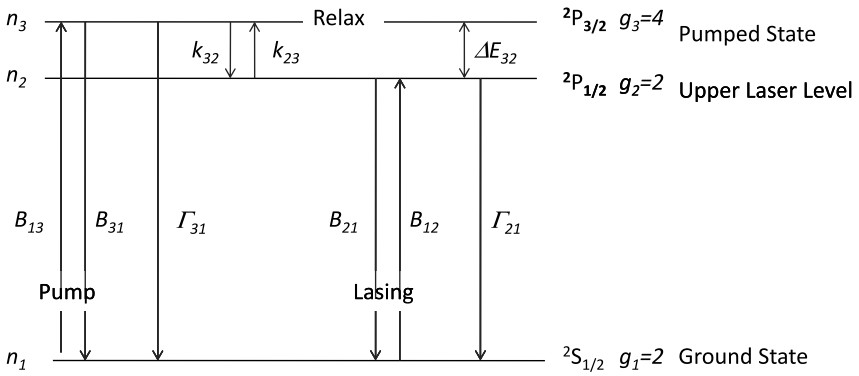

Fig. 1 Energy level diagram and key processes for the DPAL system

system has achieved 0.35 W at 81%, 10 W at 68% and 48 W (quasi-CW) with 52% efficiency [5, 9, 11].

In this paper, part I, we describe a three-level rate equation model that can be applied to longitudinal laser pumped alkali metal vapor lasers. In part I, the pump is assumed to be single frequency and provides for analytic solutions to the laser rate equations. The motivation for developing the analytic model in part I is that it is easy to use, provides for fast computations, and gives an intuitive grasp of the influence of the various laser parameters. In part II, the solution methodology developed in part I is expanded to include the more general case of broadband pumping. The model relies heavily on earlier works that were concerned with modeling three-level solid-state laser systems that are pumped longitudinally with diodes or other lasers [3, 13–16]. In the development of the plane wave model, which follows, we assume that the pump and laser beams are single frequency and centered at the peaks of the absorption and emission cross sections. The spectral distributions of the D_2 pump and D_1 lasing transitions for the 500 torr baseline calculations presented below are assumed to be single modified Lorentzians that take into account the additional broadening due to the hyperfine structure [18]. In addition, the pressure broadened absorption and emission lines are assumed to be spectrally homogeneous.

Parametric solutions for the rate equations are provided in graphical form and are centered on a specific set of baseline parameters that may be considered as representative of a number of low-power DPAL experimental papers reported in the literature [3–12]. Some important aspects of the baseline are now summarized. The sealed cell gain length is 2.0 cm, the cell temperature is 393 K corresponding to a gas phase Rb vapor pressure number density of $1.85 \times 10^{13}/\text{cm}^3$. The methane and helium densities are $9.66 \times 10^{18}/\text{cm}^3$ and $6.44 \times 10^{18}/\text{cm}^3$, corresponding to room temperature fill pressures of 300 and 200 torr respectively. When parametric variations in CH_4 density are made, the He balance is adjusted so that the total buffer density remains constant, so that the line center cross-sectional values change minimally over the range of the variation. We emphasize that the baseline parameters do not necessarily represent optimal performance. Rather the baseline parameters were selected to illustrate transition between complete pump absorption, quasi two-limit performance and the transition to pump bleaching predicted by the model.

2 Longitudinally pumped inter-cavity intensities

In the following, we develop an analytic three-level model for the end-pumped alkali metal vapor laser. The model is formulated in terms of longitudinally averaged number densities, which by definition are independent of z. The strongest support for the use of longitudinally averaged number densities comes from showing the formal equivalence of two independent mathematical approaches for describing quasi two-level end-pumped solid-state lasers reported in the 1990s [13, 14]. The first of these approaches, [13], formally integrates the rate equations for single-pass pumping with no internal losses to obtain a solution making no assumptions concerning the z dependence of any quantities contained in the rate equations. The second approach, [14], uses longitudinally averaged number densities and energy balance to extract a solution. The second approach is more flexible in the sense that it allows for double passing the pump and for the inclusion of intracavity loss terms, whereas the first approach does not. Using these two mathematical approaches for single-pass pumping with no internal loss, the authors have previously shown the formal mathematical equivalence of these two approaches for DPAL systems in the quasi two-level limit [19]. In this work, we make the assumption that the use of longitudinally averaged number densities remains a valid approximation not only for the quasi two-level limit including double-pass pumping and intracavity loss terms, but also in the parameter space that extends beyond the two-level limit to regions where the three-level nature of the system is required to explain DPAL behavior. The validity of this assumption and the resulting model must of course be tested over time as the DPAL technology advances in its ability to both explain

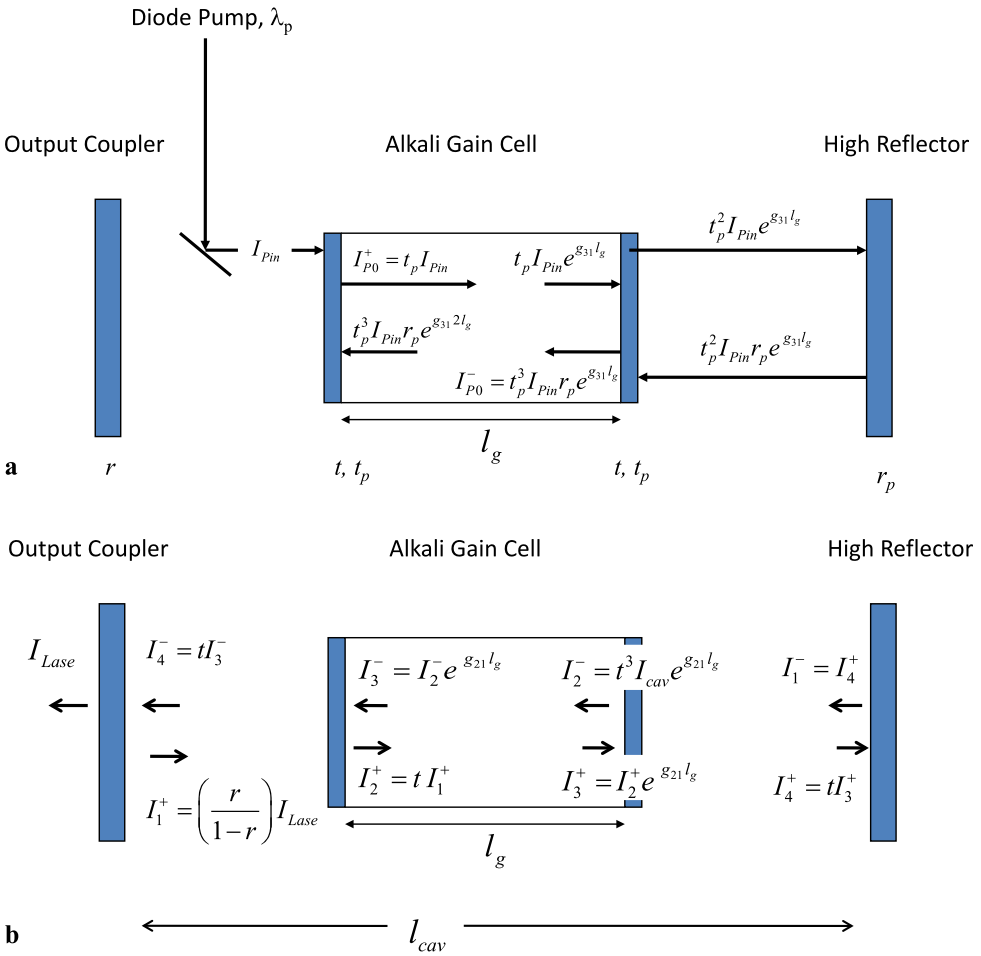

Fig. 2 Optical schematic showing (**a**) pump intensities at different cavity locations for the two-pass pump configuration; (**b**) laser intensities at different locations in the laser cavity

and organize experimental DPAL data. Having made this assumption it then becomes possible to develop expressions for the longitudinally averaged two-way pump intensity, Ω, in terms of the input pump intensity and the longitudinally averaged two-way intracavity laser circulating intensity, Ψ, in terms of the output laser intensity. The integrations involved in determining Ω and Ψ below are made tractable by assuming longitudinally averaged number densities. Using Ω and Ψ allows for the formulation of an intermediate set of rate equations that are the same at any position in the gain cell (i.e. independent of z). The rate equations formulated in terms of Ω and Ψ admit analytic algebraic solutions. Once the intermediate analytic solutions have been obtained, they are used to obtain a final solution that gives the laser output intensity in terms of the applied input pump intensity through the solution of a transcendental equation. The methodology is such that the small signal and lasing solutions for both single frequency and broadband pump sources can all be treated with the same formalism. The great advantage of working in the intermediate, analytic solution space is that the saturation characteristics of the three-level systems can be studied with analytic equations. In addition, limiting solution forms can be obtained from the analytic solutions. In particular, analytic quasi two-level equations, including expressions for the slope efficiency and threshold pump intensity, can be obtained directly from the three-level analytic equations (without solving a transcendental equation) when the spin-orbit mixing rate becomes very large. The analytic forms of the quasi two-level equations play a prominent role in the theory we present because it is in this region of rapid spin-orbit mixing where the three-level alkali laser obtains its most efficient operation.

Consider a typical geometry for an end-pumped alkali metal laser as shown schematically in Fig. 2 [12]. We envision that the pump laser at the wavelength of the D_2 transition is injected into the laser cavity through a polarizing beam splitter. The pump beam then passes through the gain cell from left to right and is reflected from the right mirror, with reflectivity r_p, back through the gain cell for a second pass. The right cavity mirror is highly reflective at both the pump and laser transition wavelengths. The gain cell windows, preferably at Brewster angle, are described by a transmission loss of t_p and t for the pump and lasing wavelengths, respectively. The laser beam, shown at the bottom of Fig. 2, resonates between the left and right hand mirrors with the useful out-coupled beam taken through the

left mirror of reflectivity, r. Also shown are the sense of the right and left traveling pump and laser beams and values for these quantities at different positions in the laser cavity. The longitudinally averaged two-way pump intensity within the gain medium is:

$$\begin{aligned}\Omega &= \left(\frac{1}{l_g}\right)\int_0^{l_g}\left(I_P^+ + I_P^-\right)dz \\ &= \frac{1}{l_g}\left(I_{P0}^+\int_0^{l_g}\mathrm{Exp}\left[\sigma_{31}\left(n_3-\frac{g_3}{g_1}n_1\right)z\right]dz\right. \\ &\quad \left. + I_{P0}^-\int_0^{l_g}\mathrm{Exp}\left[\sigma_{31}\left(n_3-\frac{g_3}{g_1}n_1\right)(l_g-z)\right]dz\right) \\ &= \left(\frac{(\mathrm{Exp}[\sigma_{31}(n_3-2n_1)l_g]-1)}{\sigma_{31}(n_3-2n_1)l_g}\right)\left(I_{P0}^+ + I_{P0}^-\right) \end{aligned} \quad (1)$$

where the intensities of the right and left traveling waves at the two ends of the gain media of length l_g are I_{P0}^+ and I_{P0}^- as illustrated in Fig. 2. The longitudinal averaged densities of the ground state n_1, upper laser level n_2, pump state n_3 and other model parameters are defined in Table 1. From Fig. 2a, the following intensity relationships can be identified:

$$\begin{aligned} I_{P0}^+ &= t_p I_{\mathrm{Pin}} \\ I_{P0}^- &= I_{\mathrm{Pin}} t_P^3 r_P e^{\sigma_{31}(n_3-2n_1)l_g} \end{aligned} \quad (2)$$

and the average pump intensity as a function of the incident pump intensity is:

$$\begin{aligned}\Omega = &\left(\frac{I_{\mathrm{Pin}}}{\sigma_{31}(n_3-2n_1)l_g}\right) \\ &\times\left(e^{\sigma_{31}(n_3-2n_1)l_g}-1\right)t_P\left(1+t_P^2 r_P e^{\sigma_{31}(n_3-2n_1)l_g}\right)\end{aligned} \quad (3)$$

For no transmission losses and complete reflection of the pump beam, (3) simplifies to

$$\Omega = \left(\frac{I_{\mathrm{Pin}}}{\sigma_{31}(n_3-2n_1)l_g}\right)\left(e^{\sigma_{31}(n_3-2n_1)2l_g}-1\right) \quad (4)$$

The pump beam will usually be highly attenuated upon a single pass of the cell and the first transmission loss could be incorporated into the incident intensity. Thus, we choose to use (4) throughout the development to simplify the expressions.

Table 1 Definition of key symbols and terms appearing in model equations

Variable	Definition
Ω	Longitudinally averaged two-way pump intensity
Ψ	Longitudinally averaged two-way laser intensity
σ_{31}	Stimulated emission cross section for pump transition evaluated at line center
σ_{21}	Stimulated emission cross section for lasing transition evaluated at line center
ν_p	Pump frequency
ν_l	Laser frequency
Γ_{31}	$\Gamma_{31} = 1/\tau_{31} + k_{31}M$
Γ_{21}	$\Gamma_{21} = 1/\tau_{21} + k_{21}M$
τ_{31}	Radiative lifetime of $^2\mathrm{P}_{3/2}$ pumped state
τ_{21}	Radiative lifetime of $^2\mathrm{P}_{1/2}$ upper laser level
k_{31}	Quenching rate coefficient for pumped state
k_{21}	Quenching rate coefficient for upper laser level
M	Concentration of collision partner (methane)
k_{32}	Rate coefficient for collisional energy transfer from $^2\mathrm{P}_{3/2}$ to $^2\mathrm{P}_{1/2}$ levels
θ	$\theta = \Delta E/k_{\mathrm{B}}T$
γ_{mix}	$\gamma_{\mathrm{mix}} = k_{32}M$
ΔE	Energy difference between $^2\mathrm{P}_{3/2}$ and $^2\mathrm{P}_{1/2}$ levels
T	Temperature
k_{B}	Boltzmann constant
l_g	Gain length
l_c	Cavity length
n	Total alkali concentration
n_1, n_2, n_3	Concentrations of $^2\mathrm{S}_{1/2}$, $^2\mathrm{P}_{1/2}$ and $^2\mathrm{P}_{3/2}$ levels, respectively
r	Output coupler mirror reflectivity
t	Window single-pass transmission

In a similar fashion, from Fig. 2b, the intracavity average two-way laser circulating intensity in the gain cell is

$$\Psi = \frac{1}{l_g}\left(I_2^+ \int_0^{l_g} \mathrm{Exp}\left[\sigma_{21}\left(n_2 - \frac{g_2}{g_1}n_1\right)z\right]dz\right) + \frac{1}{l_g}\left(I_2^- \int_0^{l_g} \mathrm{Exp}\left[\sigma_{21}\left(n_2 - \frac{g_2}{g_1}n_1\right)(l_g - z)\right]dz\right) = \left(\frac{(\mathrm{Exp}[\sigma_{21}(n_2 - n_1)l_g] - 1)}{\sigma_{21}(n_2 - n_1)l_g}\right)\left(I_2^+ + I_2^-\right) \quad (5)$$

Assuming the high reflector is also 100% reflecting for the laser (D_1) wavelength, a window transmission loss of t, and output coupler reflectivity of r, provides the intensity relationships:

$$I_2^+ = trI_4^- \quad (6)$$

$$I_2^- = \frac{I_4^-}{t\,\mathrm{Exp}[\sigma_{21}(n_2 - n_1)l_g]} \quad (7)$$

$$I_{\mathrm{Lase}} = (1 - r)I_4^- \quad (8)$$

$$I_1^+ = \frac{r}{(1 - r)}I_{\mathrm{Lase}} \quad (9)$$

as illustrated in Fig. 2. The useful output laser intensity in terms of the average two-way laser circulating intensity in the gain cell is

$$I_{\mathrm{Lase}} = \frac{\sigma_{21}(n_2 - n_1)l_g t(1 - r)\,\mathrm{Exp}[\sigma_{21}(n_2 - n_1)l_g]}{(\mathrm{Exp}[\sigma_{21}(n_2 - n_1)l_g] - 1)(1 + t^2 r\,\mathrm{Exp}[\sigma_{21}(n_2 - n_1)l_g])}\Psi \quad (10)$$

There can be a significant intensity associated with scattering and transmission losses at the windows. The intracavity circulating intensity that is lost as a result of the nonperfect window transmission, I_{Scat}, is determined by tracing the laser power reflected back into the cavity for a complete round trip (Fig. 2b). The four terms add up to give the total power loss:

$$I_{\mathrm{Scat}} = I_{\mathrm{Lase}}\left(\frac{r}{(1 - r)}\right)(1 - t)\left(1 + \mathrm{Exp}\left[\sigma_{21}(n_2 - n_1)l_g\right] \times \left(t + t^2 + t^3\,\mathrm{Exp}\left[\sigma_{21}(n_2 - n_1)l_g\right]\right)\right) \quad (11)$$

The advantages of clean, Brewster angle widows are evident.

3 Steady-state populations

The analytic model is derived from the steady-state solutions of the time-dependent rate equations for the three-level system, expressed in terms of the average intensities for the pump, Ω, and the laser, Ψ:

$$\frac{dn_1}{dt} = 0 = \sigma_{31}(n_3 - 2n_1)\frac{\Omega}{h\nu_P} + \sigma_{21}(n_2 - n_1)\frac{\Psi}{h\nu_L} + n_2\Gamma_{21} + n_3\Gamma_{31} \quad (12)$$

$$\frac{dn_2}{dt} = 0 = -\sigma_{21}(n_2 - n_1)\frac{\Psi}{h\nu_L} + \gamma_{\mathrm{mix}}\left(n_3 - 2\,\mathrm{Exp}[-\theta]n_2\right) - n_2\Gamma_{21} \quad (13)$$

$$\frac{dn_3}{dt} = 0 = -\sigma_{31}(n_3 - 2n_1)\frac{\Omega}{h\nu_P} - \gamma_{\mathrm{mix}}\left(n_3 - 2\,\mathrm{Exp}[-\theta]n_2\right) - n_3\Gamma_{31} \quad (14)$$

$$\frac{d\Psi}{dt} = 0 = \left(rt^4\,\mathrm{Exp}\left[\sigma_{21}(n_2 - n_1)2l_g\right] - 1\right)\frac{\Psi}{\tau_{\mathrm{RT}}} + \frac{n_2 c^2 \sigma_{21} h\nu_L}{l_g} \quad (15)$$

The rates for collisional transfer between the fine structure states, $\gamma_{\mathrm{mix}} = k_{32}M$, are related by detailed balance, $k_{23} = 2e^{-\theta}k_{32}$, where $\theta = \Delta E_{32}/k_{\mathrm{B}}T = 1.139$ for Rb at $T = 300$ K. The concentration of the arbitrary collision partner inducing spin-orbit relaxation, M, should be chosen high enough to prevent bottlenecking.

An examination of (12)–(14) shows that they are not linearly independent. A linearly independent set can be obtained by eliminating (14) and substituting the alkali metal number density conservation:

$$n_1 + n_2 + n_3 = n \quad (16)$$

The quantity n is the total number density of the alkali metal and is usually determined from the alkali metal vapor pressure curve.

In the steady-state treatment below, for reasons of mathematical simplicity we neglect the second term in (15). A small spontaneous emission noise term is required to start laser oscillation. By neglecting this term, we are ignoring the fact that near threshold there can be a loss in the excited state populations as the gain increases due to axially directed amplified spontaneous emission exciting the lowest loss resonator mode. Neglecting the spontaneous emission term in (15), the resulting system of equations has two solution branches, one for $\Psi = 0$ and the other for $\Psi \neq 0$. The $\Psi = 0$ solution branch is used to explain the small signal behavior when the system is below threshold. Once the threshold is reached and laser action begins, the system is described by the $\Psi \neq 0$ solution branch with the gain on the lasing transition clamped at its threshold value. For the $\Psi \neq 0$ case, (15) is equivalent to the laser threshold condition:

$$\sigma_{21}(n_2 - n_1) = g_{\mathrm{th}} = -\frac{\ln(rt^4)}{2l_g} \quad (17)$$

Table 2 Values for input parameters for baseline laser performance

Variable	Description	Value	Units	Reference
l_g	Gain length	2.0	cm	
A_{beam}	Pump beam area	1	cm^2	
n	Total Rubidium concentration	1.85×10^{13}	cm^{-3}	
[He]	Helium concentration	6.44×10^{18}	cm^{-3}	
[CH_4]	Methane concentration	9.66×10^{18}	cm^{-3}	
σ_{31}	Pump stimulated cross section	4.92×10^{-13}	cm^2	[18]
σ_{21}	Laser stimulated cross section	4.80×10^{-13}	cm^2	[18]
r	Out-coupler mirror reflectivity	0.2	–	
η_{qe}	Quantum efficiency	0.98	–	
t	Window transmission	0.975	–	
g_{th}	Threshold gain	0.428	cm^{-1}	
T	Cell temperature	393	K	
k_{32}	Spin-orbit mixing rate coefficient	3.16×10^{-10}	$\text{cm}^3\ \text{s}^{-1}$	[17]
τ_{31}	Radiative lifetime of pumped level	26.23	ns	[3]
τ_{21}	Radiative lifetime of upper laser level	27.70	ns	[3]
k_{31}, k_{21}	Quenching rate coefficients	0	$\text{cm}^3\ \text{s}^{-1}$	[20]
I_{sat}	Saturation intensity	19.8	W/cm^2	
$2e^{-\theta}$	Spin-orbit Boltzmann factor	0.84	–	
κ	Ratio of spin-orbit to radiative rates	80	–	
k_1	First spin-orbit kinetic constant	2.53	–	
k_2	Second spin-orbit kinetic constant	0.473	–	

The small-signal populations as functions of Ω are obtained by solving (12)–(14) at zero laser intensity, $\Psi = 0$:

$$n_1^0 = n\frac{\frac{\Omega}{I_{\text{sat}}}k_2 + 1}{\frac{\Omega}{I_{\text{sat}}}k_1 + 1} \tag{18}$$

$$n_2^0 = n\frac{\frac{\Omega}{I_{\text{sat}}}(k_1 - 3k_2)}{\frac{\Omega}{I_{\text{sat}}}k_1 + 1} \tag{19}$$

$$n_3^0 = n\frac{\frac{\Omega}{I_{\text{sat}}}2k_2}{\frac{\Omega}{I_{\text{sat}}}k_1 + 1} \tag{20}$$

where it is convenient to define two pressure-dependent, spin-orbit relaxation terms, as:

$$k_1 = \frac{3 + 2\kappa\frac{\Gamma_{31}}{\Gamma_{21}}(1 + 3e^{-\theta})}{1 + \kappa(1 + 2\frac{\Gamma_{31}}{\Gamma_{21}}e^{-\theta})} \tag{21}$$

$$k_2 = \frac{1 + 2\kappa\frac{\Gamma_{31}}{\Gamma_{21}}e^{-\theta}}{1 + \kappa(1 + 2\frac{\Gamma_{31}}{\Gamma_{21}}e^{-\theta})} \tag{22}$$

The saturation intensity for the pump transition is defined in the traditional manner, $I_{\text{sat}} = (h\nu_p/\sigma_{31})\Gamma_{31}$. The rate for spin-orbit relaxation relative to the decay rate for the pumped state is defined as $\kappa = k_{32}M/\Gamma_{31} = \gamma_{\text{mix}}/\Gamma_{31}$. Note that in the absence of quenching, the radiative decay rates for the two excited states are nearly identical (see Table 2): $\Gamma_{31}/\Gamma_{21} = 1.056$.

The corresponding (negative) gain on the pump transition in the absence of lasing is readily identified as

$$g_{31}^0 = \sigma_{31}\left(n_3^0 - 2n_1^0\right) = -2\sigma_{31}n\frac{1}{1 + k_1(\frac{\Omega}{I_{\text{sat}}})} \tag{23}$$

The two non-dimensional parameters of (21)–(22) provide a pressure-dependent modification to the effective saturation intensity. At low pump intensities, the expected Beer's law attenuation, $g_{31} = -2\sigma_{31}n = -\sigma_{13}n$, is obtained. For typical DPAL conditions listed in Table 2, the sample is optically thick with an absorption photon's mean free path of $\lambda_\varphi \cong 110$ μm. As with all three-level lasers, the pump rate must be highly bleached to sample and produce a population inversion.

The small-signal gain on the DPAL lasing transition depends on pump intensity as

$$g_{21}^0 = \sigma_{21}\left(n_2^0 - n_1^0\right) = \sigma_{21}n\frac{(\frac{\Omega}{I_{\text{sat}}})(k_1 - 4k_2) - 1}{(\frac{\Omega}{I_{\text{sat}}})k_1 + 1} \tag{24}$$

For high pump intensity, $\Omega/I_{\text{sat}} \gg 1$, the small signal approaches an upper bound of

$$\lim_{\Omega\to\infty} g_{21}^0 = \sigma_{21}n\left(1 - 4\frac{k_2}{k_1}\right) \tag{25}$$

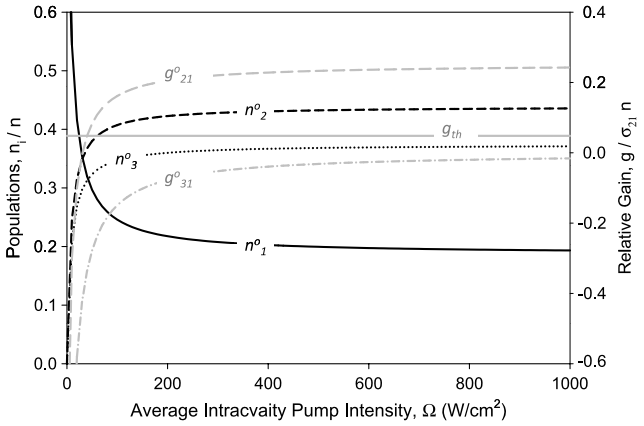

Fig. 3 The dependence of small-signal populations: (–) n_1^0, (- - -) n_2^0, and (···) n_3^0, and gain: (-·-·-) g_{31}^0 and (—) g_{21}^0, on average intracavity pump intensity

Furthermore, if the spin-orbit relaxation rate significantly exceeds the spontaneous emission rate, $\kappa \gg 1$, as needed to prevent bottlenecking, then the two excited states approach their statistical distribution and the small-signal gain attains the ideal limit of

$$g_{21}^{0,\text{ideal}} = \sigma_{21} n \frac{(1-e^{-\theta})}{(1+3e^{-\theta})} \tag{26}$$

For rubidium at room temperature, $g_{21}^{0,\text{ideal}}/\sigma_{21} n = 0.347$, and about one third of the entire alkali population is inverted.

The small-signal populations and gain as a function of average pump intensity for the baseline DPAL conditions given in Table 2 (300 torr of CH_4 and 200 torr of He at 300 K) are shown in Fig. 3. The populations approach their saturated limits for pump intensities above 200 W/cm^2, or about ten times the saturation intensity of $I_{\text{sat}} = 19.8$ W/cm^2. The n_2 and n_3 levels for the conditions given in Table 2 are populated with the ratio of $n_3^0/n_2^0 = 2k_2/(k_1 - 3k_2) = 0.851$, very near the equilibrated ratio of $(n_3^0/n_2^0)_{\text{eq}} = 2e^{-\theta} = 0.838$ at $T = 393$ K, independently of Ω. This is due to the fact that for these small-signal conditions the time constant for relaxation between the $^2P_{3/2}$ and $^2P_{1/2}$ levels is much faster than their respective radiative lifetimes, $\kappa = 80$. Absorption on the pump transition is very high with no pumping, 900%/cm. Transparency in the laser transition is achieved at about 30 W/cm^2 and the laser gain exceeds the threshold condition equation (17) at a pump intensity of about 40 W/cm^2. The asymptotic limit of the small-signal gain for the conditions given in Table 2 approaches 227%/cm. It is these very high small-signal gains and large stimulated emission cross sections that give these three-level systems their remarkable properties.

4 Bleached pump wave

Next we describe the general methodology to express the analytic solutions in terms of the externally applied measurable pump intensity, I_{Pin}. Rewriting (4) to show the explicit functional dependence on Ω yields:

$$\Omega = \left(\frac{I_{\text{Pin}}}{\sigma_{31}(n_3[\Omega] - 2n_1[\Omega])l_g}\right) \times \left(e^{\sigma_{31}(n_3[\Omega]-2n_1[\Omega])2l_g} - 1\right) \tag{27}$$

where the populations are provided for the solutions to (12)–(13), (16), presented as (18)–(20) for the no-lasing case. The equation is transcendental with readily available numerical solutions. However, for highly saturated pump conditions, the (negative) gain on the pump transition from (23) reduces to

$$\lim_{\Omega\to\infty} g_{31}^0 \equiv g_{31}^{0,\text{bleached}} = \lim_{\Omega\to\infty} \frac{-2\sigma_{31} n}{1 + (\frac{\Omega^{\text{bleached}}}{I_{\text{sat}}})k_1} = -\frac{2\sigma_{31} n}{k_1}\left(\frac{I_{\text{sat}}}{\Omega^{\text{bleached}}}\right) \tag{28}$$

Solving (27)–(28) for the average pump intensity under highly saturated (bleached) conditions yields:

$$\Omega^{\text{bleached}} = I_{\text{Pin}} \frac{(-4\frac{\sigma_{31} n l_g}{k_1})(\frac{I_{\text{sat}}}{I_{\text{Pin}}})}{\ln[1 - 2\frac{\sigma_{31} n l_g}{k_1}(\frac{I_{\text{sat}}}{I_{\text{Pin}}})]} \tag{29}$$

If the path length is not too large, $l_g < (k_1/2\sigma_{31} n)(I_{\text{Pin}}/I_{\text{sat}})$, so that the bleached wave extends beyond the end of the cell, then the logarithm in the denominator can be approximated by the leading term in the Taylor series so that

$$\Omega^{\text{bleached}} \cong 2I_{\text{Pin}} - \left(\frac{\sigma_{31} n l_g}{k_1}\right) I_{\text{sat}} \tag{30}$$

If nearly all the pump intensity is absorbed in this linear region over the double path, then the average pump intensity is equal to the incident value, $\Omega^{\text{bleached}} \to I_{\text{Pin}}$. If the sample is highly bleached so that the pump is barely attenuated, then the two-way average intensity is twice the incident intensity.

The more general numerical solution to (27) as a function of input pump intensity for the baseline conditions of Table 2 is shown in Fig. 4. For small values of I_{Pin} the pump does not fully penetrate the medium on the forward pass. The input pump is completely absorbed in a small fraction of the cell length l_g and the longitudinal average is small. When I_{Pin} reaches approximately 225 W/cm^2, the sample becomes fully bleached and Ω begins to see the effect of the reflected pump beam. When I_{Pin} reaches approximately 230 W/cm^2, the slope of the Ω vs. I_{Pin} curve reaches its maximum value and from then on decreases approaching an asymptotic value of ~2 at $I_{\text{Pin}} = 1000$ W/cm^2. For input intensities of

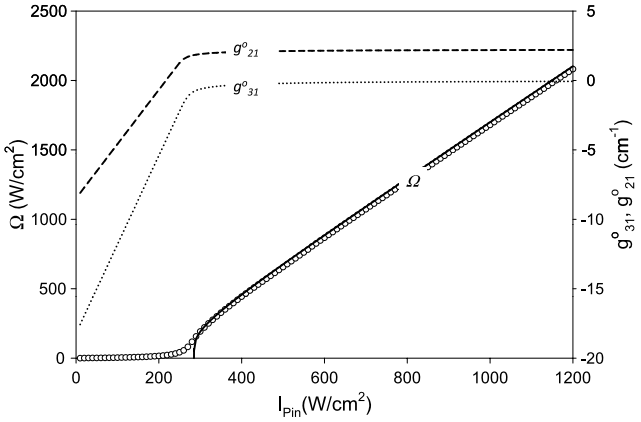

Fig. 4 (○) Numerical solution to (27) for the average intracavity pump intensity compared with (–) the approximated bleached solution of (29) for the $\Psi = 0$, no-lasing case. The small signal (···) absorption on the pump transition and (- - -) gain for the lasing transition as a function of input pump intensity are also shown

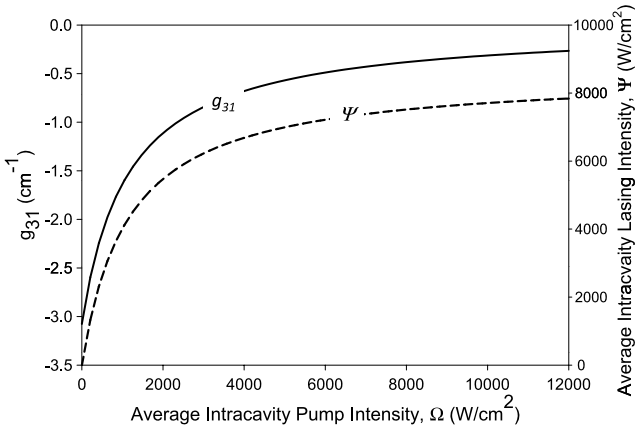

Fig. 5 (–) Absorption on pump transition and (- - -) average intracavity laser intensity as a function of average pump intensity. Threshold occurs at $\Omega = 40.04$ W/cm^2

300 W/cm^2 and above, the medium is largely bleached with the additional power above 300 W/cm^2 transmitted through the medium. Figure 4 also demonstrates that the approximation of (30) is appropriate for $I_{\rm Pin} > 300$ W/cm^2.

Figure 4 also illustrates the small-signal absorption on the pump transition and gain for the lasing transition as a function of input pump intensity. Both g_{31} and g_{21} increase linearly to $I_{\rm Pin} \sim 250$ W/cm^2 at which point the slopes change rapidly as the pump transition saturates. At this point the gain medium is bleached and becomes largely transparent to increases in pump intensity. Threshold of (17) is reached when $I_{\rm Pin}$ is 237.7 W/cm^2 producing an average two-way circulating intensity of $\Omega = 40.3$ W/cm^2.

5 Gain saturation and lasing intensity

The laser intensity is determined by the requirement that the population inversion be reduced from the small signal, unsaturated value of (24), to the threshold value expressed by (17). The populations in the presence of lasing are derived by simultaneously solving (12)–(13), (16)–(17), yielding:

$$n_1 = \frac{[\frac{1}{2}(n - \frac{g_{\rm th}}{\sigma_{21}})(1+\kappa) - (\frac{g_{\rm th}}{\sigma_{21}})\kappa e^{-\theta}] + \frac{1}{2}(n - \frac{g_{\rm th}}{\sigma_{21}})(\frac{\Omega}{I_{\rm sat}})}{1 + \kappa(1+e^{-\theta}) + 2(\frac{\Omega}{I_{\rm sat}})} \tag{31}$$

$$n_2 = \frac{\frac{1}{2}(n + \frac{g_{\rm th}}{\sigma_{21}})(1+\kappa) + \frac{1}{2}(n + \frac{3g_{\rm th}}{\sigma_{21}})(\frac{\Omega}{I_{\rm sat}})}{1 + \kappa(1+e^{-\theta}) + 2(\frac{\Omega}{I_{\rm sat}})} \tag{32}$$

$$n_3 = \frac{(n + \frac{g_{\rm th}}{\sigma_{21}})(\kappa e^{-\theta}) + (n - \frac{g_{\rm th}}{\sigma_{21}})(\frac{\Omega}{I_{\rm sat}})}{1 + \kappa(1+e^{-\theta}) + 2(\frac{\Omega}{I_{\rm sat}})} \tag{33}$$

The saturated absorption on the pump transition is

$$g_{31} = \sigma_{31}(n_3 - 2n_1) = -\sigma_{31} n \frac{(1+\kappa-\kappa e^{-\theta}) - \frac{g_{\rm th}}{\sigma_{21} n}(1+\kappa+3\kappa e^{-\theta})}{[1+\kappa(1+e^{-\theta}) + 2(\frac{\Omega}{I_{\rm sat}})]} \tag{34}$$

The absorption is much greater in the presence of lasing, as the atoms rapidly cycle through the coupled pump and lasing processes. For the conditions of Table 2 at high pump intensities, the absorption in the case without lasing from (23) is 24 times less than with lasing.

The corresponding averaged intracavity laser intensity is

$$\Psi = \eta_0 I_{\rm sat}\left(\alpha \frac{\Omega}{I_{\rm sat}} - \beta\right) \tag{35}$$

where

$$\alpha \equiv \frac{(\frac{\sigma_{21} n}{g_{\rm th}})(2\kappa(1-e^{-\theta})(\frac{\Gamma_{31}}{\Gamma_{21}}) - 1) - (3 + 2(1+3e^{-\theta})\kappa(\frac{\Gamma_{31}}{\Gamma_{21}}))}{2[(1+\kappa(1+e^{-\theta})) + 2\frac{\Omega}{I_{\rm sat}}]} \tag{36}$$

$$\beta \equiv \left(1 + \frac{\sigma_{21} n}{g_{\rm th}}\right)\left[\frac{1+\kappa(1+2(\frac{\Gamma_{31}}{\Gamma_{21}})e^{-\theta})}{2[(1+\kappa(1+e^{-\theta})) + 2\frac{\Omega}{I_{\rm sat}}]}\right] \tag{37}$$

Defining the efficiency, $\eta_0 \equiv \eta_{\rm qe}(\Gamma_{21}\sigma_{31}/\Gamma_{31}\sigma_{21})$, establishes the connection to the quantum efficiency, $\eta_{\rm qe} = \nu_L/\nu_P$.

Solutions for the intracavity two-way average laser circulating intensity, Ψ, and absorption on the pump transition, g_{31}, as a function of average pump rate are illustrated in Fig. 5 for the baseline conditions of Table 2. The intracavity laser intensity rises sharply initially and then gently begins to roll over, beginning at an average pump intensity of $\Omega \sim 1000$ W/cm^2. The absorption exhibits essentially the same shape. A comparison with the small signal, $\Psi = 0$ case in Fig. 3, shows the difference in the degrees of saturation

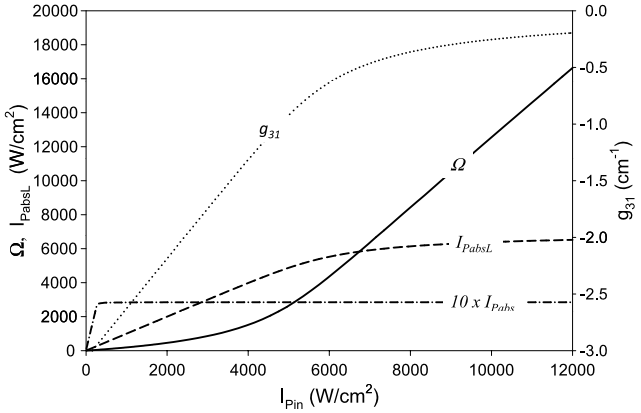

Fig. 6 (–) Intracavity pump intensity and (· · ·) pump absorption coefficient, g_{31}, a function of incident pump intensity for the conditions of Table 2. Absorbed power (- - -) with lasing and (·-·-·) 10× absorbed power without lasing illustrate the dramatic increase in absorption when lasing occurs

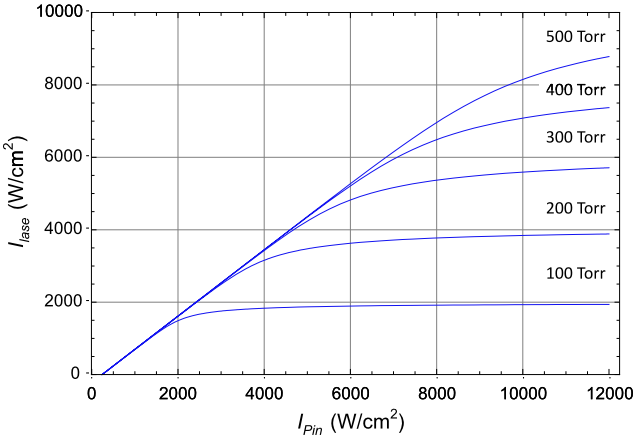

Fig. 7 Laser output intensity as a function of input pump intensity for a family of ethane pressures, illustrating the need for higher spin-orbit relaxation rates at high pump intensity

at $\Omega = 1000$ W/cm^2. For the small-signal conditions the g_{31} pump transition is essentially saturated at 1000 W/cm^2 whereas for the lasing conditions this same degree of saturation is not achieved until Ω is approximately 12000 W/cm^2. In the small signal case the loss rate of the upper levels is due only to spontaneous emission whereas for the lasing case stimulated emission also depopulates the upper levels and can occur at much higher rates. For lasing conditions the Rb atoms are cycling and processing the pump photons through the processes of absorption on the 1–3 transition, collisional relaxation from the 3–2 levels, and stimulated emission on the 2–1 transition. They can do this at extremely high rates limited by the slowest step in the cycle, which is the collisional transfer rate between the 3 and 2 levels.

This effect is most clearly evident when expressing the analytic laser equations in terms I_{Pin} and I_{Lase}. Numerically solving the transcendental equation (27) using the saturated lasing populations of (31)–(33), provides the longitudinally averaged pump intensity, Ω, and pump absorption, g_{31}, as a function of input intensity, as shown in Fig. 6. The power absorbed for the lasing case I_{PabsL}:

$$I_{\mathrm{PabsL}} = -I_{\mathrm{Pin}}\left(e^{g_{31}[I_{\mathrm{Pin}}]2l_g} - 1\right) \tag{38}$$

is contrasted with the zero laser intensity case in Fig. 6. The slope of the absorption vs. IPin is one up to powers of ~5000 W/cm^2 and this region is identified as the linear absorption region (i.e. complete pump absorption). As I_{Pin} increases above 5000 W/cm^2, the slope decreases approaching a value of zero at $I_{\mathrm{Pin}} = 12000$ W/cm^2. This effect as we show below is due to the fact that the slow step in the laser cycling process, the net collisional transfer rate between levels 3 and 2, has been reached.

Equation (35) specifies the average intracavity laser intensity, which is transformed to the input intensity via (10):

$$I_{\mathrm{Lase}} = \frac{\Psi[I_{\mathrm{Pin}}]g_{\mathrm{th}}l_g e^{g_{\mathrm{th}}l_g}t(1-r)}{(e^{g_{\mathrm{th}}l_g}-1)(1+t^2re^{g_{\mathrm{th}}l_g})} \tag{39}$$

A set of parametric plots of I_{Lase} vs. I_{Pin}, where the density of the methane relaxant species has been varied from 100 torr to 500 torr in steps of 100 torr, and the total pressure is held constant at 500 torr, is provided in Fig. 7. The effect of bleaching with increasing values of I_{Pin} is clearly evident. It is the rate-limiting process of collisionally induced energy transfer between the $^2P_{3/2}$ and $^2P_{1/2}$ states in the three-step lasing cycle that is responsible for this effect. As the density of the methane relaxant species is increased, the relaxation rate increases and the onset of bleaching moves progressively to higher values of I_{Pin}. From a laser design standpoint, given an input pump intensity, the relaxant methane density can always selected with a high enough value so that the device will operate in the linear slope regime. The point at which the rollover begins to occur is also reflected in changes in the ratio of n_3/n_2 from its equilibrium value, as shown in Fig. 8. Near threshold the ratio of n_3/n_2 for all relaxant pressures is close to the equilibrium value. As I_{Pin} increases, the ratio increases and appears to asymptotically approach, for all pressure values, to a value that is roughly twice the equilibrium value as the medium becomes saturated.

For conditions in which collisional relaxation is not rate-limiting (i.e. at low-input pump intensities), the initial slope of the I_{Lase} vs. I_{Pin} curves depends on the intracavity window transmission loss factor t, as illustrated in Fig. 9. The intracavity lasing intensity produced by stimulated emission is partitioned between the useful output laser intensity and the intensity that is lost as a result of the non-perfect window transmission. As the window transmission factor t decreases

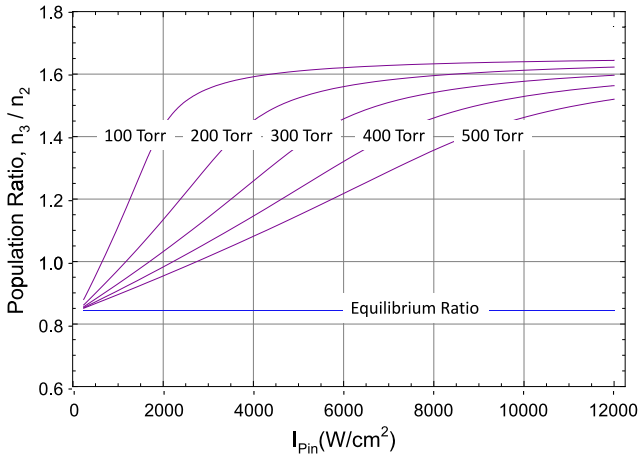

Fig. 8 Populations ratio for pumped and upper laser levels as a function of incident pump intensity for a family of ethane pressures. The equilibrated ratio at $T = 393$ K is $(n_3^0/n_2^0)_{\text{eq}} = 2e^{-\theta} = 0.838$

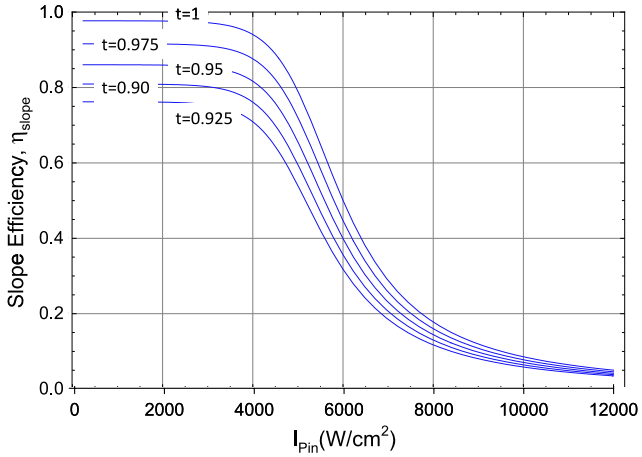

Fig. 9 The effect of cavity losses on slope efficiency

from a value of unity, a larger fraction of the circulating intensity is dissipated as scattering loss. Shown in Fig. 9 is a set of five parametric curves in which the window transmission factor, t, has been reduced in steps of 0.025 from $t = 1$ to 0.9. All other parameters for the curves shown have the values given in Table 2. For $t = 1$, the initial slope efficiency achieves the quantum limit of 98.2%. As transmission decreases from a value of unity, the slope decreases. For the baseline condition $t = 0.975$ the slope is 0.92 and for $t = 0.9$ the slope has decreased to 0.765.

There is another factor that can contribute to the experimentally observed slope. It results from considerations that are not contained in the rate equation model and due to the fractional spatial overlap of the gain and laser resonator mode intensity volumes, termed η_{mode}, the mode-matching efficiency [20]. The general expression for η_{mode} is given by

$$\eta_{\text{mode}} = \frac{\int g_{21}(x,y,z) I_{\text{res}}(x,y,z)\,dx\,dy\,dz}{\int I_{\text{res}}^2(x,y,z)\,dx\,dy\,dz} \tag{40}$$

The three-dimensional spatial distribution of the gain on the lasing transition $g_{21}(x, y, z)$ is interrogated only in regions where the three-dimensional spatial laser mode intensity distribution $I_{\text{res}}(x, y, z)$ is significant. A value of η_{mode} of less than unity indicates that part of the inversion will decay by spontaneous emission and quenching if present and not by stimulated emission. In the rate equation model under consideration we treat η_{mode} as an adjustable or fitting parameter when comparisons are made with experimental data. The mode-matching efficiency η_{mode} is incorporated in the rate equation model by multiplying (38) by η_{mode}:

$$I_{\text{Lase}} = \frac{\eta_{\text{mode}} \Psi[I_{\text{Pin}}] g_{\text{th}} l_g e^{g_{\text{th}} l_g} t(1-r)}{(e^{g_{\text{th}} l_g} - 1)(1 + t^2 r e^{g_{\text{th}} l_g})} \tag{41}$$

We interpret η_{mode} as representing the resonator extraction efficiency. Its effect is to reduce the useful output laser intensity and the laser slope efficiency. For the baseline laser conditions with $\eta_{\text{mode}} = 0.8$, the useful power is reduced with a slope efficiency of 0.74.

In this final part of the rate-equation model development section, we discuss briefly the energy balance. The energy balance equations are complimentary to the rate-equation model solutions and are useful in interpreting experimental data and in particular for the calculation of thermal loads. Examination of the energy level diagram and the kinetic and radiative processes defined in Fig. 1 shows there are only four places the absorbed pump energy can go:

$$P_{\text{Abs}} = P_{\text{Lase}} + P_{\text{Scat}} + P_{\text{rad}} + P_{\text{therm}} \tag{42}$$

where, in the presence of lasing,

$$P_{\text{Lase}} = \frac{A_{\text{beam}} \Psi[I_{\text{Pin}}] g_{\text{th}} l_g e^{g_{\text{th}} l_g} t(1-r)}{(e^{g_{\text{th}} l_g} - 1)(1 + t^2 r e^{g_{\text{th}} l_g})} \tag{43}$$

$$P_{\text{Scat}} = A_{\text{beam}} I_{\text{Lase}} \left(\frac{r(1-t)}{1-r} \right) \left(1 + e^{g_{\text{th}} l_g} \left(t + t^2 + t^3 e^{g_{\text{th}} l_g}\right)\right) \tag{44}$$

$$P_{\text{rad}} = \left(\frac{n_3[I_{\text{Pin}}] h\nu_P}{\tau_{31}} + \frac{n_2[I_{\text{Pin}}] h\nu_L}{\tau_{21}} \right) V_L \tag{45}$$

$$P_{\text{therm}} = k_{32} M \left(n_3[I_{\text{Pin}}] - 2e^{-\theta} n_2[I_{\text{Pin}}]\right) h(\nu_P - \nu_L) V_L \tag{46}$$

The laser volume, V_L, is defined by the pump beam area A_{beam} times the gain length, l_g. The term P_{rad} gives the power that is radiated by spontaneous emission in the laser volume, and the term P_{therm} gives the thermal power developed in the laser volume as a result of the energy defect in the three-level systems. The thermal load would increase dramatically if quenching contributed to the deactivation.

6 Fine structure mixing and quasi two-level limit

Under conditions where the spin-orbit relaxation rate is large relative to both the excited state lifetime, $\gamma_{\text{mix}} \gg \Gamma_{31}$ or $\kappa \gg 1$, and the absorption rate, $\kappa = \gamma_{\text{mix}}/\Gamma_{31} \gg \Omega/I_{\text{sat}}$, the two excited states, $^2P_{1/2}$ and $^2P_{3/2}$, are equilibrated: $n_3/n_2 = 2e^{-\theta}$. These conditions are readily achievable and represent ideal laser operation. Otherwise, bottlenecking occurs between the two upper states, limiting the rate of optical conversion. This quasi two-level (Q2L) laser limit can be indentified from the general three-level result by allowing $\kappa \to \infty$. The absorption on the pump transition from (34) in the Q2L limit becomes

$$\lim_{\kappa\to\infty} g_{31} \equiv g_{31}^{\text{Q2L}} = -\sigma_{31} n \left[\frac{(1-e^{-\theta}) - \frac{g_{\text{th}}}{\sigma_{21} n}(1+3e^{-\theta})}{(1+e^{-\theta})} \right] \tag{47}$$

The transcendental equation (4) for the longitudinally averaged pump intensity is directly solved when the pump absorption is independent of pump intensity, as in (47), yielding

$$\Omega^{\text{Q2L}} = I_{\text{Pin}} \left(\frac{e^{2 g_{31}^{\text{Q2L}} l_g} - 1}{g_{31}^{\text{Q2L}} l_g} \right) \tag{48}$$

The two parameters in the averaged intracavity laser intensity of (35) become

$$\lim_{\kappa\to\infty} \alpha \equiv \alpha^{\text{Q2L}} = \frac{(\frac{\sigma_{21} n}{g_{\text{th}}})(2(1-e^{-\theta})(\frac{\Gamma_{31}}{\Gamma_{21}})) - (2(1+3e^{-\theta})(\frac{\Gamma_{31}}{\Gamma_{21}}))}{2(1+e^{-\theta})} \tag{49}$$

$$\lim_{\kappa\to\infty} \beta \equiv \beta^{\text{Q2L}} = \left(1 + \frac{\sigma_{21} n}{g_{\text{th}}}\right) \left[\frac{1 + 2(\frac{\Gamma_{31}}{\Gamma_{21}}) e^{-\theta}}{2(1+e^{-\theta})} \right] \tag{50}$$

Finally, the laser intensity of (41) becomes

$$I_{\text{Lase}}^{Q2l} = \eta_{\text{slope}} I_{\text{Pin}} - I_{\text{th}} \tag{51}$$

where

$$\eta_{\text{slope}} = \eta_{\text{qe}} \eta_{\text{mode}} \left(\frac{1-r}{rt} \right) \left[\frac{(1 - e^{2 g_{31}^{\text{Q2L}} l_g})}{(e^{g_{\text{th}} l_g} - 1)(t^2 e^{g_{\text{th}} l_g} + 1)} \right] \tag{52}$$

$$I_{\text{th}} = \left(\frac{h\nu_p l_g}{\tau} \right) \left(\frac{1}{1 - e^{2 g_{31}^{\text{Q2L}} l_g}} \right) \left(n + \frac{g_{\text{th}}}{\sigma_{21}} \right) \left(\frac{1 + 2e^{-\theta}}{2(1+e^{-\theta})} \right) \tag{53}$$

The effective lifetime of the spin-orbit equilibrated upper states, τ, has been identified as

$$\frac{1}{\tau} = (1-f)\Gamma_{31} + f\Gamma_{21} = \Gamma_{21} \left(\frac{1 + 2\frac{\Gamma_{31}}{\Gamma_{21}} e^{-\theta}}{1 + 2e^{-\theta}} \right) \tag{54}$$

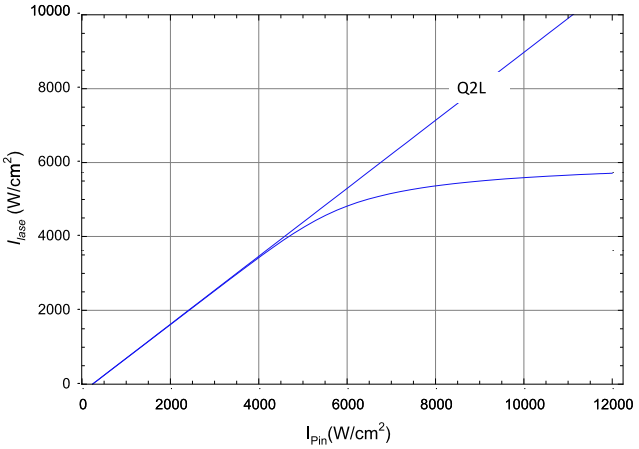

Fig. 10 Comparison of three-level and quasi two-level models for their conditions of Table 2

where the fraction of the population in the upper laser level is

$$f \equiv \lim_{\kappa\to\infty} \frac{n_2}{n_2 + n_3} = \frac{1}{1 + 2e^{-\theta}} \tag{55}$$

Note that the threshold intensity is proportional to the product of the saturation intensity and the ideal small signal, often interpreted as the maximum output intensity:

$$I_{\text{max}} \equiv I_{\text{sat}} g_{21}^{0,\text{ideal}} l_g = \left(\frac{h\nu_p}{\sigma_{21}\tau} \right) \sigma_{21} n l_g \left(\frac{1-e^{-\theta}}{1+3e^{-\theta}} \right) \tag{56}$$

Threshold in the DPAL system is large. However, the output intensity is not limited by the product of (56). As pump intensity increases, the cycle rate for an individual atom increases and the output power continues to scale linearly.

A comparison of these quasi two-level solutions to the more general three-level solutions is provided in Fig. 10 for the conditions of Table 2. The agreement is excellent in the linear regime where the pump intensities are <4 kW/cm^2. If the methane concentration is increased so that the spin-orbit relaxation rate competes favorably with the stimulated rates, then the performance of the Q2L can be regained. Indeed, the DPAL system performs according to the Q2L when then gain medium is properly designed.

In steady state, the three-level DPAL model requires that the rates for pumping, spin-orbit relaxation, and lasing be nearly equilibrated (to within the rates for spontaneous emission and quenching). When the mixing rate becomes small and the Q2L is not obtained, laser performance is rather sensitive to relaxer gas and alkali concentration. For example, the scaling of laser intensity with pump intensity for several alkali atom concentrations for the conditions of Table 2 is illustrated in Fig. 11. In some recent DPAL demonstrations, these concentrations and/or transverse density variations may be adversely affected by spatially evolving temperatures, reducing system efficiency. However, by

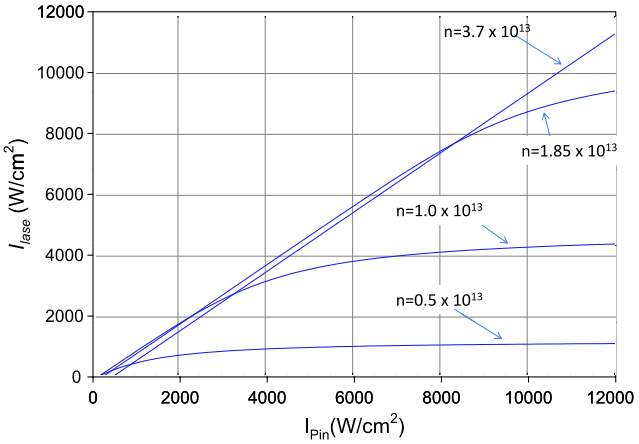

Fig. 11 Comparison of laser performance for several alkali concentrations for the conditions of Table 2 except $t = 1$

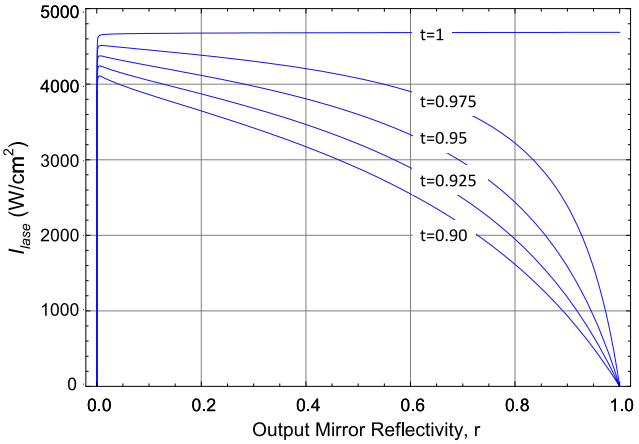

Fig. 12 Quasi two-level laser power for $I_{\mathrm{Pin}} = 5\ \mathrm{kW/cm^2}$ as a function of output coupler reflectivity for several cavity transmission losses

appropriate redesign of the relaxation kinetics, high performance near the Q2L limit should be recoverable.

Finally, optimal output coupling fractions can be easily identified in the quasi two-level limit, as illustrated in Fig. 12. For no cavity transmission loss, $t = 1$, the output power is insensitive to output coupling fraction, due to the very high gain. However, intracavity loss dramatically alters the laser saturation characteristics and maximum performance is achieved for low-output coupler reflectivity.

7 Conclusions

The ideal performance of the Diode Pumped Alkali Laser (DPAL) system is well described by a simple quasi two-level model with longitudinally averaged number densities. The slope efficiency depends primarily on the fraction of pump energy absorbed and cavity transmission losses, assuming ideal resonator and pump mode overlap. Threshold is achieved when the sample is fully bleached and optical losses are exceeded. Threshold is adversely affected by quenching. The maximum small-signal inversion approaches one third of the total Rb concentration under highly saturated pump conditions. At high pump intensities, $>1\ \mathrm{kW/cm^2}$, the pumped and upper laser levels show significant deviations from the statistical distribution for spin-orbit relaxer pressures of less than 1 atmosphere. However, the quasi two-level model adequately predicts laser output power for pump intensities as high as $8\ \mathrm{kW/cm^2}$ for 500 torr of methane relaxer. Absorption of pump energy is strongly affected by the presence of the laser field. Indeed, saturation is never achieved in the quasi two-level limit in the presence of lasing. The saturation intensity modified by the spin-orbit relaxation rates has been developed. The current results are limited to narrowband pump sources. A full analysis of the pressure-broadened, hyperfine split absorption cross section convolved with a spectrally broad diode pump source will be presented in a subsequent paper.

References

1. W.F. Krupke, R.J. Beach, V.K. Kanz, S.A. Payne, Opt. Lett. **28**, 2336 (2003)
2. P. Rabinowitz, S. Jacobs, G. Gould, Appl. Opt. **1**, 513 (1962)
3. R.J. Beach, W.F. Krupke, V.K. Kanz, S.A. Payne, M.A. Dubinski, L.D. Merkle, J. Opt. Soc. Am. B **21**, 2151 (2004)
4. T. Ehrenreich, B. Zhdanov, T. Takekoshi, S.P. Phipps, R.J. Knize, Electron. Lett. **41**, 7 (2005)
5. B.V. Zhdanov, T. Ehrenreich, R.J. Knize, Opt. Commun. **260**, 696 (2006)
6. R.H. Page, R.J. Beach, V.K. Kanz, W.F. Krupke, Opt. Lett. **31**, 353 (2006)
7. Y. Wang, T. Kasamatsu, Y. Zheng, H. Miyajima, H. Fukuoka, S. Matsuoka, M. Niigaki, H. Kubomura, T. Hiruma, H. Kan, Appl. Phys. Lett. **88**, 141112 (2006)
8. T.A. Perschbacher, D.A. Hostutler, T.M. Shay, in *XVI International Symposium on Gas Flow and Chemical Lasers & High Power Laser Conference*, Gmunden, Austria (2006)
9. B. Zhdanov, R.J. Knize, Opt. Lett. **15**, 2167 (2007)
10. B. Zhdanov, C. Maes, T. Ehrenreich, A. Havko, N. Koval, T. Meeker, B. Worker, B. Flusche, R.J. Knize, Opt. Commun. **270**, 353 (2007)
11. B.V. Zhdanov, J. Sell, R.J. Knize, Electron. Lett. **44**, 582 (2008)
12. B.V. Zhdanov, A. Stooke, G. Boyadjian, A. Voci, R.J. Knize, Opt. Lett. **33**, 414 (2008)
13. P. Peterson, A. Gavrielides, P.M. Sharma, Opt. Commun. **109**, 282 (1994)
14. R.J. Beach, Opt. Commun. **123**, 385 (1995)
15. T.Y. Fan, R.L. Byer, IEEE J. Quantum Electron. **QE-23**, 605 (1987)
16. W.P. Risk, J. Opt. Soc. Am. B **5**, 1412 (1988)
17. M.D. Rotondaro, G.P. Perram, J. Quant. Spectrosc. Radiat. Transf. **57**, 497 (1997)
18. G.A. Pitz, G.P. Perram, SPIE Proc. **7005**, 700526 (2008)
19. G.D. Hager, J. McIver, D. Hostutler, G. Pitz, G.P. Perram, SPIE Proc. **7005**, 700528 (2008)
20. E.S. Hrycyshyn, L. Krause, Can. J. Phys. **48**, 2761 (1970)